Seasonal Variability in Local Carbon Dioxide Combustion Sources over the Central and Eastern US using Airborne In-Situ Enhancement Ratios

Joshua P. DiGangi[1], Yonghoon Choi[1,2], John B. Nowak[1], Hannah S. Halliday[1,3*], Glenn S. Diskin[1], Sha Feng[4,], Zachary R. Barkley[4], Thomas Lauvaux[4,***], Sandip Pal[5], Kenneth J. Davis[4], Bianca C. Baier[6,7], Colm Sweeney[7]**

[1] NASA Langley Research Center, Hampton, VA, USA.

[2] Science Systems and Applications, Inc., Hampton, VA, USA.

[3] Universities Space Research Association, Columbia, MD, USA.

[4] The Pennsylvania State University, University Park, PA, USA

[5] Department of Geosciences, Atmospheric Science Division, Texas Tech University, Lubbock, TX, USA

[6] Cooperative Institute for Research in Environmental Sciences, University of Colorado-Boulder, Boulder, CO, USA

[7] NOAA Earth System Research Laboratory, Boulder, CO, USA

[*] Now at: US EPA Research Triangle Park, Durham, NC, USA

[**] Now at: Atmospheric Sciences and Global Change Division, Pacific Northwest National Laboratory, Richland, WA, USA

[***] Now at: LSCE/IPSL, Gif sur Yvette, France

Corresponding author: Joshua P. DiGangi (joshua.p.digangi@nasa.gov)

Key Points

- Airborne CO & CO_2 enhancement ratios used to examine distribution of CO_2 emissions by combustion source efficiency
- Discrepancies observed between model & airborne results in seasonal & regional behavior in biomass:fossil fuel burning CO_2 emission ratios
- Satellite fire data suggests discrepancies may be partially due to mix of spatial resolution and biomass/fire parameterization

Abstract

We present observations of local enhancements in carbon dioxide (CO_2) from local emissions sources over three eastern US regions during four deployments of the Atmospheric Carbon Transport-America (ACT-America) campaign between summer 2016 and spring 2018. Local CO_2 emissions were characterized by carbon monoxide (CO) to CO_2 enhancement ratios (i.e. $\Delta CO/\Delta CO_2$) in airmass mixing observed during aircraft transects within the atmospheric boundary layer. By analyzing regional-scale variability of CO_2 enhancements as a function of $\Delta CO/\Delta CO_2$ enhancement ratios, observed relative contributions to CO_2 emissions were contrasted between different combustion regimes across regions and seasons. Ninety percent of observed summer combustion in all regions was attributed to high efficiency fossil fuel (FF) combustion ($\Delta CO/\Delta CO_2$ < 0.5%). In other seasons, regional contributions increased from less efficient forms of FF combustion ($\Delta CO/\Delta CO_2$ 0.5-2%) to as much as 60% of observed combustion. CO_2 emission contributions attributed to biomass burning (BB) ($\Delta CO/\Delta CO_2$ > 4%) were negligible during summer and fall in all regions, but climbed to 10-12% of observed combustion in the South during winter and spring. Vulcan v3 CO_2 2015 emission analysis showed increases in residential and commercial sectors seasonally matching increases in less efficient FF combustion, but could not explain regional trends. WRF-Chem modeling, driven by CarbonTracker CO_2 fire emissions, matched observed winter and spring BB contributions, but conflictingly predicted similar levels of BB during fall. Satellite fire data from MODIS and VIIRS suggested higher spatial resolution fire data might improve modeled BB emissions.

1 Introduction

Carbon dioxide (CO_2) is a direct product of fossil fuel combustion and a relatively inert compound in the atmosphere making it a good tracer of anthropogenic emissions, which collectively have a strong influence on regional air quality and global climate. Accurately quantifying the accumulation of atmospheric CO_2 from its broad variety of sources is critical to predicting future trends in global temperature and climate. Models utilize emissions inventories of CO_2, combined with ocean and land biosphere models, to predict its transport and accumulation in the atmosphere. Thus, the proper apportionment and quantification of emission sources is important in order for models to predict future behavior. For CO_2, combustion is one of the primary anthropogenic sources, but sources range widely in terms of both spatial distribution and emission type (Gurney

et al., 2020a). In particular, biomass burning (BB) remains a difficult source to constrain due to its often unpredictable timing and wide variety of vegetative fuels. As a result, emission inventories must be continuously validated through direct measurements. Tower networks enable vital long term, continuous, high accuracy records of CO_2 levels, but are limited in spatial coverage. Satellite measurements provide global coverage, but with limited spatial and temporal resolution, as well as limited comparability with in situ measurements (Eldering et al., 2017; Yokota et al., 2009). Airborne measurements of CO_2 bridge these two spatial regimes, providing data with high spatial resolution and comparability over a broad area, making them well suited for regional emissions surveys.

Carbon monoxide (CO) is a ubiquitous carbon oxidation intermediate with an atmospheric lifetime on the order of weeks to months and is the chemical precursor to gas-phase CO_2 formation (Holloway et al., 2000). While the primary source of CO is through combustion, other sources include direct biological emission and oxidation of volatile organic compounds (VOCs) (Griffin et al., 2007). Ratios of CO vs CO_2 ($\Delta CO/\Delta CO_2$) are particularly powerful for evaluating fossil fuel CO_2 sources, as the ratio of a plume from a single point source provides information about the source's combustion efficiency (CE). High efficiency (fuel-lean, high temperature) combustion produces relatively little CO, as the fuel carbon is nearly completely converted to CO_2. Low efficiency (fuel-rich, lower temperature) combustion converts less of the fuel carbon to CO_2, resulting in the release of greater amounts of intermediate combustion products, such as CO and organic compounds. For example, vehicular emissions in the United States typically have emission ratios in the range of < 2% $\Delta CO/\Delta CO_2$ (Djuricin et al., 2010; Graven et al., 2009; LaFranchi et al., 2013; Turnbull et al., 2011), whereas modern power plant emissions typically are much more efficient, less than < 0.1% $\Delta CO/\Delta CO_2$ (Peischl et al., 2010; USEPA, 2010). BB emissions typically have emission ratios on the order of 4% or higher $\Delta CO/\Delta CO_2$ (Akagi et al., 2011; Andreae & Merlet, 2001; Suntharalingam et al., 2004), which makes $\Delta CO/\Delta CO_2$ enhancement ratios a reliable marker for distinguishing uncontrolled BB from controlled fossil fuel (FF) combustion.

In this work, we describe seasonal airborne measurements of CO_2 and CO, as well as a statistical examination of their plume enhancements, in multiple regions over the central and eastern United States. We apply a technique reported by Halliday et al. (2019) which utilized enhancement ratios of $CO:CO_2$ to examine relative combustion regime contributions and sources, expanding these

methods in order to ascertain contributions to local CO_2 emissions. This methodology provides a bottom-up perspective of the influence of various combustion sources on CO_2 emissions with respect to the inferred CE, allowing for apportionment between BB and FF emissions. These results are then compared to modeled CO_2 source contributions and satellite fire products in order to evaluate the model response with respect to season and region in the eastern half of the United States.

2 Materials and Methods

2.1 ACT-America

The Atmospheric Carbon Transport-America (ACT-America) campaign was a NASA Earth Venture Suborbital project focused on reducing errors in inversion models of the transport and emissions of atmospheric carbon dioxide and methane over the continental United States (Davis et al., 2020; Wei et al., 2020). ACT-America consisted of seasonal six-week intensives with three deployments per intensive; sampling locations and dates are shown in Table 1. Each deployment sampled over three separate regions, as shown in the campaign flight tracks in Fig. 1. Measurements were collected using two aircraft: the NASA Wallops Flight Facility C-130 (N436NA) and the NASA Langley Research Center B-200 King Air (N529NA). The C-130 was instrumented with in situ chemistry measurements (Kostinek et al., 2019), whole air sampling (Baier et al., 2020), and remote sensing measurements (Campbell et al., 2020; Pal et al., 2020). The B-200 was instrumented with only in situ measurements (Weibring et al., 2020) and whole air sampling measurements. The two aircraft combined to collect a mixture of planetary boundary layer (PBL), and lower & upper free tropospheric data. Three types of flight patterns were flown: frontal passage flights aimed at describing the transport of greenhouse gases (GHGs) by midlatitude cyclones (Pal et al., 2020), fair weather flights aimed at constraining regional fluxes, and OCO-2 validation flights aimed at quantifying CO_2 levels over multiple altitudes under an OCO-2 satellite track (Bell et al., 2020). Flight patterns primarily focused on level altitude legs at either 300 m above ground level (AGL) for PBL measurements or constant pressure altitude flight levels above the PBL ranging up to 9 km MSL. Flights were conducted primarily in midday conditions. While flights were at times conducted in areas with broad, regional plumes, individual sources were not targeted.

Campaign	Sampling Dates		
	Mid-Atlantic	**Midwest**	**South**
Summer 2016	18 July to 1 August	1-16 August	16-29 August
Winter 2017	27 February to 10 March	13-27 February	30 January to 13 February
Fall 2017	3-16 October	16-30 October	30 October to 13 November
Spring 2018	4-20 May	23 April to 8 May	12-23 April

Table 1. ACT-America flight dates by season and nominal region.

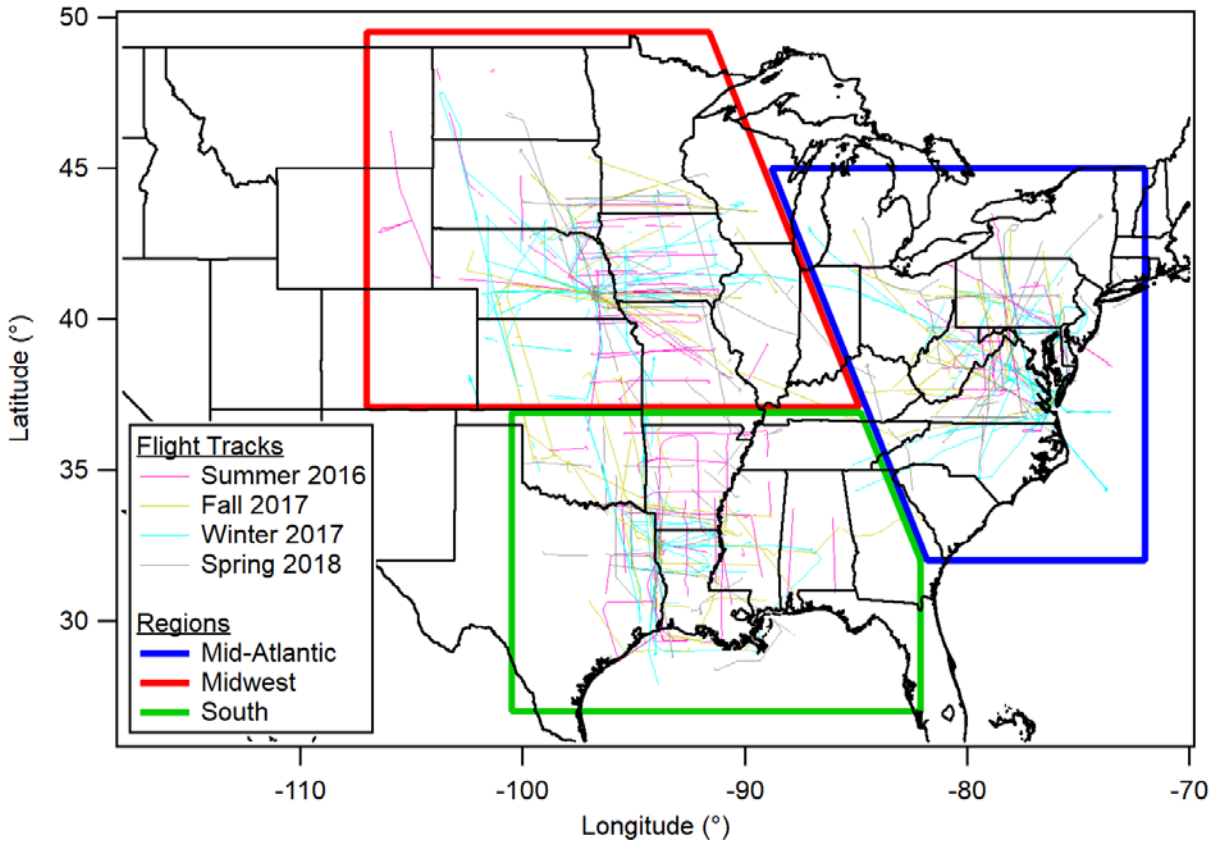

Figure 1. Map of ACT-America flight domains. All flight tracks at < 1 km AGL for each season. Colored boxes denote the regions defined in this study. The border between the Midwest and South regions was 37°N, while the border between the Mid-Atlantic region and the other two was a line drawn between 45°N, 89°W and 32°N, 82°W.

2.2 In-Situ Airborne Measurements

The two aircraft contained identical payloads for measuring in situ gas phase carbon species. CO_2, CO, and methane (CH_4) dry mole fractions were measured using a commercial cavity ringdown spectrometer (G2401-m, PICARRO, Inc.) with a custom gas sampling & calibration system (Fig. S1). Air was sampled through a commercial stainless steel total air temperature probe modified for gas sampling (Buck Research Instruments, LLC). The probe extended 12” outboard from the fuselage to avoid aircraft boundary layer contamination. Sampled air was dried using a commercial

Nafion dryer tube (PD-200T-24, Permapure, Inc.) then passed through a flow controller maintaining a constant 1.5 standard liter per minute (SLM) total flow. The sample was then compressed to a constant ~1050 mbar, from which the spectrometer sampled at 0.5 SLM, with the remaining flow exhausted to the cabin using an absolute proportional pressure relief valve set at ~1065 mbar. With the exception of the Nafion dryer, all inlet materials were stainless steel to minimized sample contamination through gas permeability. The spectrometer cycled between measurements of each species, along with a measurement of the remaining water in the gas sample, sequentially every 2.5 s. The instrument temporal through the gas system and instrument was measured to be typically ~2-3 s. Calibration gas was introduced through a solenoid valve upstream of the dryer at 2 SLM, with the excess flow exhausted through the inlet to ensure that only calibrant was sampled. By introducing the calibrant before the Nafion dryer, the dry calibration gas was humidified to the same level as the dried ambient air (typically 0.03-0.05%), thus avoiding water vapor-dependent calibration discrepancies (Reum et al., 2019). Single concentration calibrations were performed hourly during flight to assess instrument offsets. Slope calibrations were conducted weekly on the ground through three-point calibrations over a broader concentration range. All calibration gases were traceable to the CO_2 X2007 (Tans et al., 2017), CO X2014A (Novelli et al., 1991), and CH_4 X2004A (Dlugokencky et al., 2005) WMO scales (NOAA ESRL). Measurement precision was 0.1 ppm, 5 ppb, and 1 ppb in 2.5 s for CO_2, CO, and CH_4, respectively. Measurement accuracy was 0.1 ppm, 2%, and 1 ppb for CO_2, CO, and CH_4, respectively.

2.3 Airborne $\Delta CO/\Delta CO_2$ Enhancement Analysis

$\Delta CO/\Delta CO_2$ were derived from using a short-term sliding slope window (Halliday et al., 2019; Smith et al., 2015). Using a sliding fixed-time bin window over the CO and CO_2 time series measured at ~2.5 s intervals and binned at 5 s intervals, a linear regression of CO vs CO_2 is calculated for each period. This results in a $\Delta CO/\Delta CO_2$ slope and a coefficient of determination (r^2), where r^2 can then be used to filter uncorrelated bins that do not represent identifiable mixing. The resulting values can then be displayed as a distribution of slopes representative of the mixing observed over certain regions and/or timescales.

For this work, running-bin linear regressions of $\Delta CO/\Delta CO_2$ were calculated using weighted orthogonal distance regression (ODRPACK95 - IGOR Pro v7;Wu & Yu, 2018), where fit mole fractions were weighted by the measurement precisions of 0.1 ppm for CO_2 and 5 ppb for CO.

Values of $\Delta CO/\Delta CO_2$ were calculated using data from the ACT-America 5 s merge (Davis et al., 2018). In Halliday et al. (2019), while the overall r^2 cutoff and bin window size significantly affected the raw frequency of observations, the normalized distribution was mostly insensitive to both of these factors. To estimate the variability that does exist, sensitivity tests were performed for each parameter over a range of r^2 values (0.3, 0.4, 0.5, 0.6, 0.7, 0.8) and bin windows (30 s, 45 s, 60 s, 90 s, 120 s), for a total of 30 different values. As the aircraft ground speed typically varied from 100-120 m/s at these altitudes, the spatial extent of the bin windows varied between 3-14 km. Figure S2 shows line histograms of the distribution of $\Delta CO/\Delta CO_2$ observed during the winter campaign. In Fig. 2a-b data are shown filtered by different r^2 cutoffs at a constant 60 s bin size, while in fig 2c-d, data are shown filtered by different bin window sizes at a constant r^2 cutoff of 0.6. Figure 2a and 2c show distributions of the frequencies of the raw number of each occurrence, while Fig. 2b and 2d show these distributions normalized by the total number of observed intercepts. The results were similar to those shown in Halliday et al. (2019), with wide variability in the absolute frequency distribution intensities, but very similar normalized frequencies regardless of parameter value.

To examine the relationship between CO_2 and CE, an extension of the technique is required. Thus, each observed slope was binned by both $\Delta CO/\Delta CO_2$ and the total ΔCO_2 in the bin, the latter used as a metric for the CO_2 intensity of the emission. The result is a 2D heat map representing the enhancement in CO_2 as a function of $\Delta CO/\Delta CO_2$ enhancement ratio (Fig. 2a). To calculate the ΔCO_2-weighted distribution with respect to $\Delta CO/\Delta CO_2$, the data were summed with respect to ΔCO_2 for each $\Delta CO/\Delta CO_2$ bin:

$$NWF\left(\left(\frac{\Delta CO}{\Delta CO_2}\right)_j\right) = 100\% * \frac{\sum_i n_{i,j} * \Delta CO_{2,i}\left(\left(\frac{\Delta CO}{\Delta CO_2}\right)_j\right)}{\sum_j \sum_i n_{i,j} * \Delta CO_{2,i}\left(\left(\frac{\Delta CO}{\Delta CO_2}\right)_j\right)} \quad (1)$$

where NWF is the normalized ΔCO_2-weighted bin frequency as a function of $\Delta CO/\Delta CO_2$ while $n_{i,j}$ is the number of points in the ith bin of ΔCO_2 and the jth bin of $\Delta CO/\Delta CO_2$. Figure 2b the resultant NWF for the measurements collected during the winter campaign. The same sensitivity

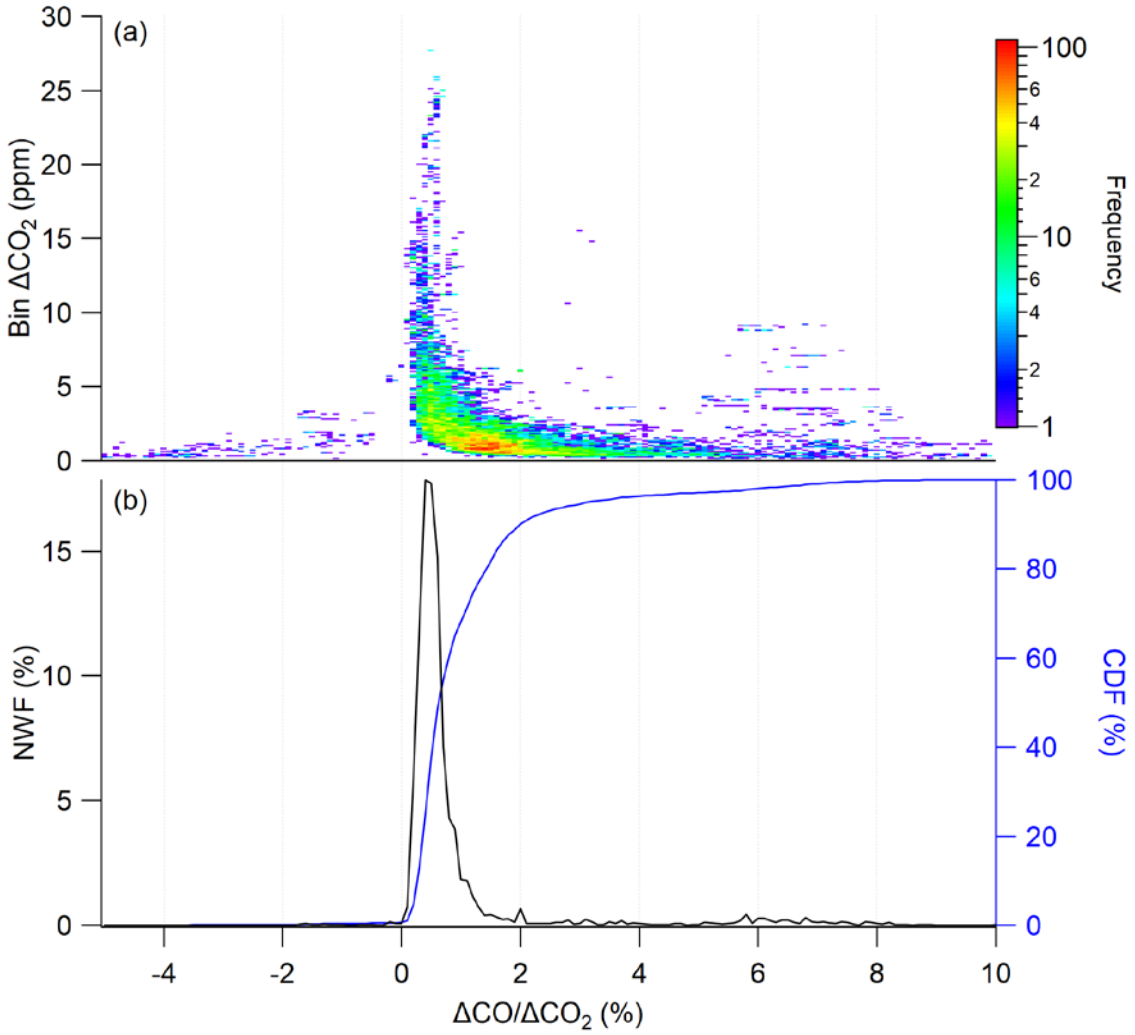

Figure 2. (a) Example heat map of plume frequency binned by ΔCO_2 and by $\Delta CO/\Delta CO_2$ slope from the winter 2017 deployment with 0.6 r^2 cutoff and a 60 s rolling bin window. (b) NWF and cumulative distribution function (CDF) of CO_2 contributions in above panel with respect to $\Delta CO/\Delta CO_2$.

analyses to r^2 and bin width were performed as with the unweighted normalized method. NWF values were mostly insensitive to the choice of r^2 cutoff and bin size (Fig. S3), though with somewhat more variability than the unweighted method. Thus, the final NWF value was calculated as the average of the 30 values from the sensitivity analyses over the different combinations of r^2 and bin width parameters, with the 1s standard deviation representing the error attributed to these cutoff choices. Instrument error was neglected for the NWF analysis (other than in the fits), as it is a relatively small contribution compared to the cutoff error (Halliday et al., 2019).

One of the key advantages of this technique is that, by focusing on $\Delta CO/\Delta CO_2$ slopes, it does not rely on other assumptions about background levels of CO and CO_2. As a result, CO and CO_2

background mole fractions are neglected entirely. An important caveat of the technique is that very high CE sources with very low $\Delta CO/\Delta CO_2$ emission ratios could be missed if the measured enhancements were below the instrument precision. In addition, this technique does not describe the total amount of CO_2 emissions, only the relative contributions nearby point of sources with different enhancement ratios from the background. Thus, the technique can be seen as internally consistent across seasons, well suited at looking at differences in contributions by CE, but not a good predictor of absolute CO_2 emissions from BB and FF combustion. A near-field source would be observed as much stronger contribution than a more distant source, making the method more biased toward near-field sources. This should be somewhat mitigated by the tendency for more distant plumes to have broadened signatures, which would translate to a greater count frequency, albeit weaker, provided it has a significantly different ratio from the background. This mitigation should be less effective at higher bin widths, which may account for some of the greater variability in the ΔCO_2-weighted NWF compared to the unweighted normalized frequency. This same effect makes it impossible to define an exact receptor footprint for the results, other than this weighting effect on source distance.

2.4 CO_2 Inversion Model

Modeled BB CO_2 source contributions were simulated by WRF-Chem v3.6.1 with the modification described in Lauvaux et al. (2012) to transport greenhouse gases as passive tracers with the consideration of conservation of mass (Butler et al., 2020). CO_2 fire flux components were obtained from NOAA's CarbonTracker products: CT2017 (Peters et al., 2005) for the summer 2016 campaign and CT-Near Real Time (NRT) 2019v2 (Peters et al., 2005) for the other 3 seasons. For simplicity, all CarbonTracker versions will be hereby referred to as CT. These CT fire emission fluxes were calculated with 3 h time resolution and 1° latitude by 1° longitude spatial resolution. The CT fire module models pyrogenic CO_2 emissions using the GFED4.1s and GEFD_CMS fire module (Giglio et al., 2013; van der Werf et al., 2017), which uses MODIS 1° fire products to detect fires and the CASA model to convert burned area to a CO_2 flux. The WRF-Chem simulation was run at hourly and 27 km^2 resolutions over North America, driven with the ERA5 reanalysis as meteorological initial and boundary conditions, and then nudged to ERA5 for better transport constraints. Choices of the model physics parameterizations used in this experiment are documented as the baseline setup in Feng et al. (2019a,b).

2.5 Vulcan CO_2 Emissions Inventory

Modeled FF CO_2 emissions were calculated using the Vulcan v3.0 emissions inventory (Gurney et al., 2020a). The Vulcan inventory provides hourly CO_2 emissions at 1 km^2 resolution for the years 2010 – 2015 (Gurney et al., 2020b). CO_2 emissions are separated into 10 sectors: onroad (vehicles), electricity production, residential, nonroad (offroad vehicles), airport, commercial, industrial, commercial marine vehicles, rail, and cement. Emission data were sourced from various inventories, primarily the US Environmental Protection Agency National Emission Inventory. For comparison with the WRF-Chem model results in this analysis, the 2015 hourly 1 km^2 Vulcan emissions were averaged spatially to the same 27 km^2 grid. Vulcan emissions were also averaged temporally between 0900 – 1700 local time to align with the aircraft flight times and minimize any biasing effects of the diurnal cycle of CO_2 emissions (Turnbull et al., 2015).

3 Results

NWF is weighted by the magnitude of the enhancement in CO_2, and thus relative NWF values can be compared at various enhancement ratios to evaluate the relative contributions of those CO_2 emission sources and their inferred combustion efficiencies. Table 2 summarizes the different regimes of $\Delta CO/\Delta CO_2$ values chosen for this work and their source assignments. These regime delineations were informed overall by cited emissions literature, but were primarily chosen for a means of consistent comparison of regime contributions across domains and campaigns. $\Delta CO/\Delta CO_2$ values less than 0% are associated with mixing with air influenced by CO_2 uptake, as non-photochemical CO sinks are not known to be common. In particular, these negative enhance ment ratios have been hypothesized to be associated with ecosystem uptake (Halliday et al., 2019; Silva et al., 2013) with either a photochemical or a well-mixed anthropogenic CO source. Values

$\Delta CO/\Delta CO_2$ Enhancement Ratio	**Source Regime**	**Regime Label**	**Typical Sources**
< 0%	Uptake-influenced mixing	-	Old pollution with biogenic uptake influence
0 – 0.5%	Very high efficiency fossil fuels	$FF_{0\text{-}0.5\%}$	Electricity generation, industry, cars
0.5 – 1%	High efficiency fossil fuels	$FF_{0.5\text{-}1\%}$	Higher efficiency vehicular
1 – 2%	Low efficiency fossil fuel	$FF_{1\text{-}2\%}$	Lower efficiency vehicular
2 – 4%	Very low efficiency fossil fuel	$FF_{2\text{-}4\%}$	Heating combustion, non-controlled vehicle emissions, and off-road combustion
> 4%	Biomass burning	$BB_{>4\%}$	Agriculture, vegetative fires

Table 2. Summary of NWF regimes.

between 0-0.5% were attributed to very high efficiency fossil fuel ($FF_{0\text{-}0.5\%}$) combustion, between 0.5-1% were attributed to high efficiency fossil fuel ($FF_{0.5\text{-}1\%}$) combustion, and between 1-2% were attributed to low efficiency fossil fuel ($FF_{1\text{-}2\%}$) combustion. $\Delta CO/\Delta CO_2$ values between 2-4% were attributed to a very low efficiency combustion regime ($FF_{2\text{-}4\%}$), as they are too low to typically be considered BB but are fairly high for typical FF combustion in the United States. Finally, values greater than 4% were attributed to biomass burning ($BB_{>4\%}$) combustion.

CO_2 uptake contributions could contribute to the positive regimes if the CO_2 uptake source is also a CO sink, and these cases would be indistinguishable from combustion plumes with this technique. However, to the best of the authors' knowledge, such a CO sink does not exist on any scale as to significantly alter our findings. Biological uptake also generally occurs on scales larger than the small window (3-10 km) observed with this technique, and the signal from this uptake would primarily be represented in the background. Efficient controlled combustion of non-fossil fuels (e.g. high-temperature wood fired furnace) could result in lower enhancement ratios akin to those typically expected for FF (Venkataraman & Rao, 2001), while inefficient combustion of FF (e.g. uncontrolled open oil burning) could result in higher enhancement ratios akin to those expected from BB (Middlebrook et al., 2012). These sources are relatively rare compared with the ubiquity of typical FF and BB combustion and thus will be neglected for the purposes of this analysis.

3.1 Seasonal $\Delta CO/\Delta CO_2$ variability

Figure 3 shows the NWF vs $\Delta CO/\Delta CO_2$ slope distribution for each deployment during different seasons, while Table S1 shows the numerical NWF contributions in each regime. In order to focus on the relative enhancement ratios of local sources in the PBL, all data above 1 km AGL were rejected in order to focus on the 300 m level altitude flight legs. NWF contributions from negative $\Delta CO/\Delta CO_2$ slopes peaked during the summer campaign, exhibited lesser contributions in spring and fall respectively, and were almost negligible in winter. This behavior is consistent with the expected levels of CO_2 biogenic uptake in each season. As a result, this negative $\Delta CO/\Delta CO_2$ slope regime will be neglected for the reminder of the analysis. The inset in Fig. 3 shows the relative NWF contributions with respect to only the positive $\Delta CO/\Delta CO_2$ regimes; numerical values can be found in Tab. S2. $FF_{0\text{-}0.5\%}$ combustion contributions were consistently the majority in all regions, particularly in summer where it constitutes over 90% of the non-negative $\Delta CO/\Delta CO_2$ slopes. The

dominance of this signal is consistent with the year-round use of most FF-based combustion. The second largest positive regime is $FF_{0.5\text{-}1\%}$, which is largest during winter, smallest during summer, and with fall and spring similar and in the middle. This correlates colder seasons with an increase in this slightly lower efficiency category of FF combustion, and the trend for all of the other $\Delta CO/\Delta CO_2$ regimes is similar. This is particularly striking for $BB_{>4\%}$, where the NWF contribution is effectively negligible during summer, very small in fall, but almost 5% and 3% of the non-negative $\Delta CO/\Delta CO_2$ slopes in winter and spring respectively. This finding is consistent with observations during the campaign, as agricultural fires in particular were observed to be common especially during the winter campaign.

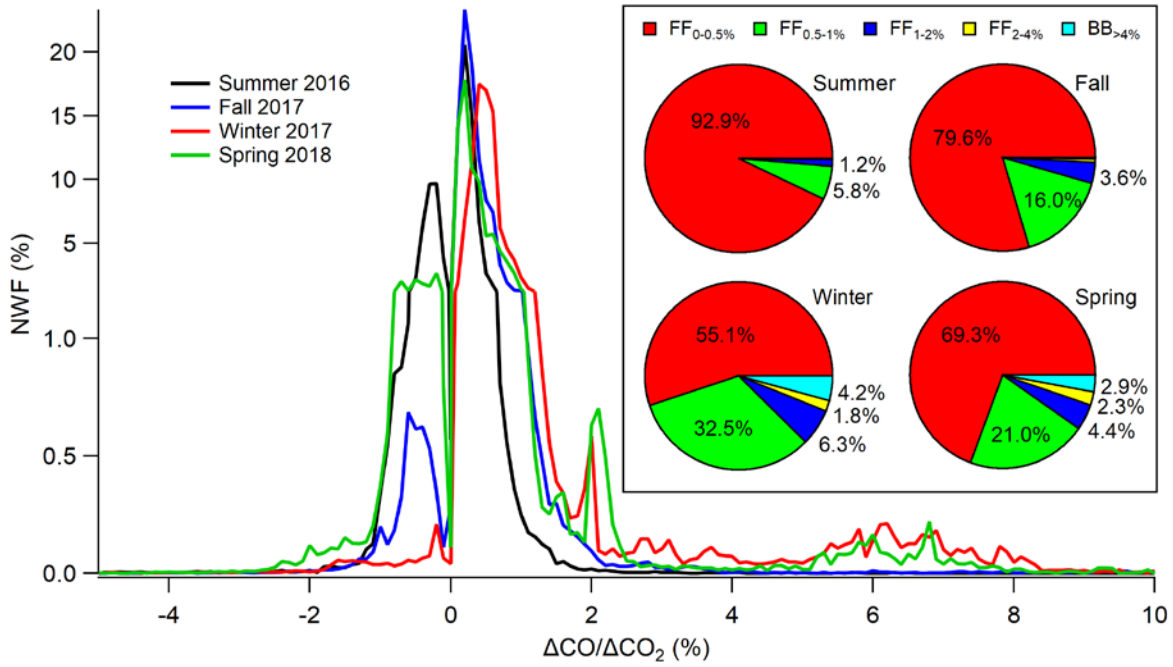

Figure 3. NWF vs $\Delta CO/\Delta CO_2$ for PBL (< 1 km AGL) for each season. (inset) Positive NWF contributions for each $\Delta CO/\Delta CO_2$ regime for each season. Regime contributions less than 1% of total are not labeled.

3.2 Regional $\Delta CO/\Delta CO_2$ variability

Observed enhancement ratios were also segregated into three ACT-America flight domains: Mid Atlantic, Midwest, and South (Fig. 1). To show the relative effects only attributed to combustion, we analyzed only the positive $\Delta CO/\Delta CO_2$ slope relative NWF contributions for each regime within the PBL (Fig. 4). During summer, all regions look very similar, each with over 90% of positive NWF contributions in the $FF_{0\text{-}0.5\%}$ combustion regime. Fall contributions differ by

region somewhat more, with a shift in the Midwestern and Southern region toward $FF_{0.5\text{-}1\%}$ and $FF_{1\text{-}2\%}$, an effect slightly stronger for the Midwestern region. This stronger influence of less efficient FF combustion could be attributed to agricultural activities, where more intensive use of heavy-duty diesel agricultural equipment during harvest leads to an increase in lower efficiency $FF_{0.5\text{-}1\%}$ and $FF_{1\text{-}2\%}$ emissions. For example, Ban-Weiss et al. (2008) observed a factor of 3.2 higher average CO emission from medium and light duty diesel vehicles compared to light duty gasoline vehicles. Increases in $FF_{0.5\text{-}1\%}$ and $FF_{1\text{-}2\%}$ were weaker in the Mid-Atlantic region, possibly due to a higher level of Midwestern agricultural activity.

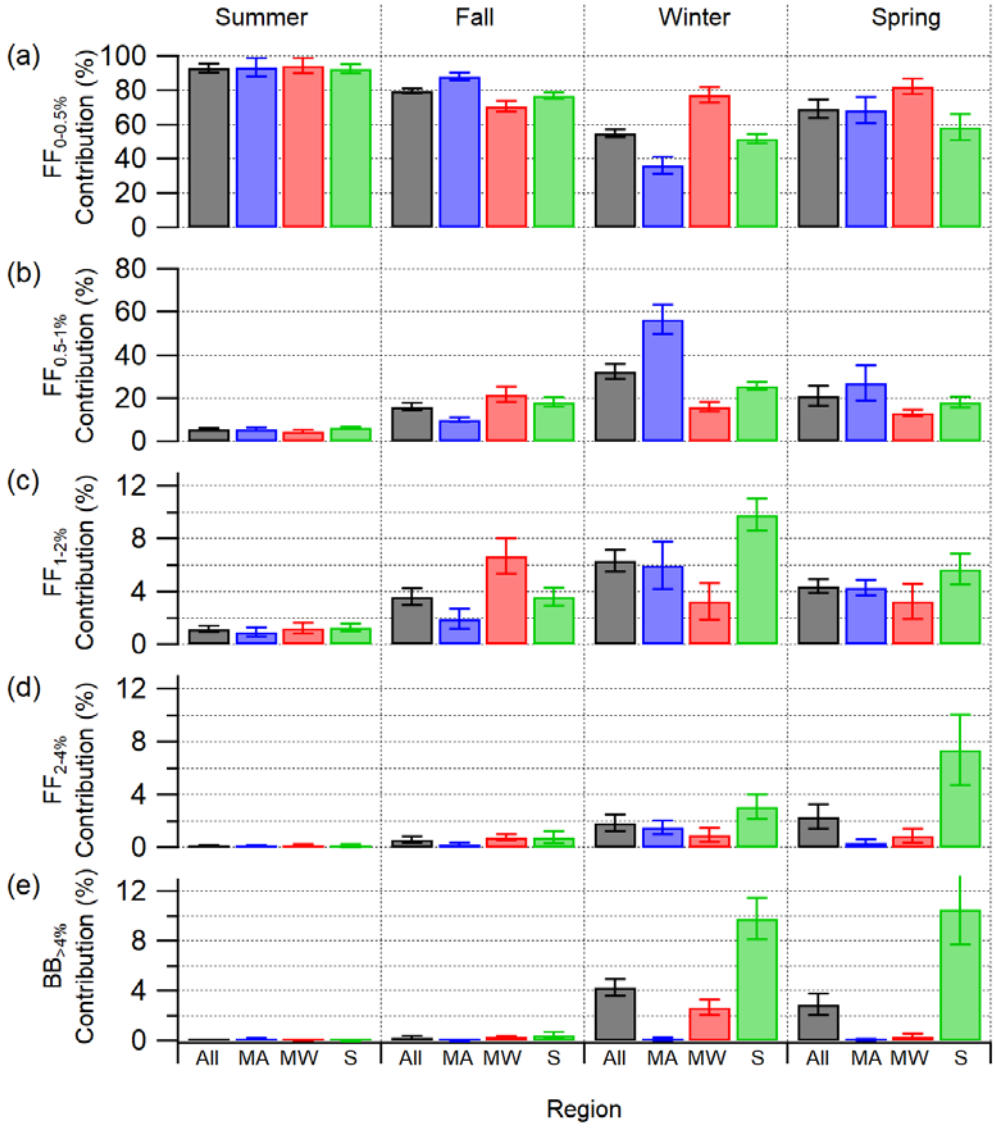

Figure 4. NWF contributions reweighted using only positive $\Delta CO/\Delta CO_2$ slope frequencies separated by season and region (MA-Mid-Atlantic, MW-Midwest, S-South) measured in the PBL (< 1 km AGL) for the (a) $FF_{0\text{-}0.5\%}$, (b) $FF_{0.5\text{-}1\%}$, (c) $FF_{1\text{-}2\%}$, (d) $FF_{2\text{-}4\%}$, and (e) $BB_{>4\%}$ regimes. Error bars denote the 1σ variability in the r^2 and bin size sensitivity analyses.

The greatest variation in combustion regime contributions is seen during the winter season. The majority of Mid-Atlantic contributions come from $FF_{0.5\text{-}1\%}$, a striking shift from the summer and fall seasons which were dominated by $FF_{0\text{-}0.5\%}$. Including the associated small increase in $FF_{1\text{-}2\%}$, over 60% of observed plume contributions were from these less efficient FF combustion categories. One contributing factor could be higher vehicular CO emissions which are seen at lower ambient temperatures (Bishop & Stedman, 1990). In contrast, the distribution of Midwestern contributions was more like that of fall, with the exception of a slight increase in $BB_{>4\%}$. The Southern region saw strong winter increases in $FF_{1\text{-}2\%}$ and $BB_{>4\%}$, each contributing 10% of the NWF. This increase in BB is consistent with an increase in wintertime agricultural burning, common in the Southeastern US (see Sect 4.3).

In the spring, Mid-Atlantic $FF_{0\text{-}0.5\%}$ was lower than in the summer and fall, but this regime once again contributed the majority of the NWF, with the F regime contributing roughly half to the NWF as seen during winter. Midwestern combustion contributions exhibited behavior similar to that during winter but with near zero $BB_{>4\%}$ influence. The lack of biomass burning is likely due to both warmer weather and the start of the planting season, during which comparatively little agricultural burning would be likely to occur. Southern contributions were very similar to those during the winter, with the biggest difference being a slight shift from $FF_{0.5\text{-}1\%}$ and $FF_{1\text{-}2\%}$ to increased $BB_{>4\%}$ and $FF_{2\text{-}4\%}$ contributions. As agricultural burning in the South is typically focused during the late fall & winter months before the early spring planting season (McCarty et al., 2007), the similarity of spring $BB_{>4\%}$ to those during winter indicates a longer burning season than anticipated.

4 Discussion

4.1 Vulcan CO_2 Fossil Fuel Emissions Comparison

Data from each sector in the Vulcan inventory (Gurney et al., 2020b) were spatially averaged to 27 km^2 and interpolated at 5 s intervals along ACT-America flight tracks below 1 km AGL. Figure 5 shows these interpolated local emissions, averaged by region for each season, with numerical values listed in Tab. S3. Emissions from each sector were then normalized by the total Vulcan emission for that region/season in order to compare with the normalized airborne data. As the analyzed Vulcan emissions were from the most recent year of the inventory, 2015, we assumed

that regional and seasonal trends in emissions persist in the years 2016 - 2018. While total annual emissions vary from year to year, relative sector contributions, as discussed here, are more likely to remain constant over the timeframe of a few years (Gurney et al., 2020a).

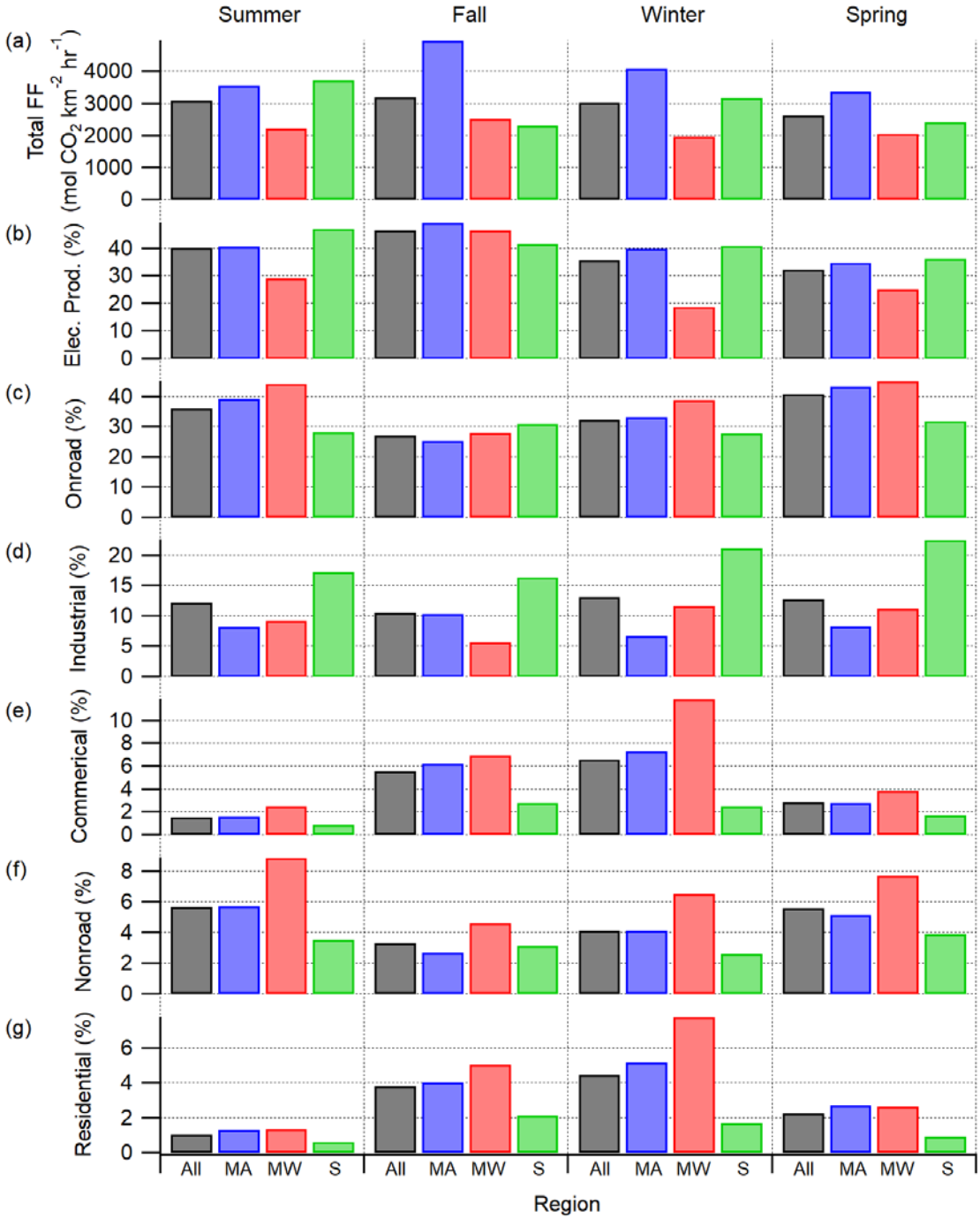

Figure 5. Averaged 27 km^2 Vulcan FF emissions along flight track below 1 km AGL. (a) Average of total emissions for all sectors. (b-g) Average emissions from each sector normalized by the average total emissions.

In all regions, total Vulcan emissions in all regions were relatively flat with respect to season, though some seasonal variability in individual regions. In the Mid-Atlantic region, total FF emissions in the fall were found to be ~45% higher than in the spring and summer, while in winter, emissions were 15-20% higher than in spring and summer. Midwestern total FF emissions were lowest in winter and spring, ~10% higher in summer, and ~25% higher in fall. Southern total emissions were at a minimum in the fall and spring, ~35% higher in winter, and ~60% higher in summer.

By sector, electricity production and onroad vehicle emissions (Fig. 5b-c) were dominant, with the plurality of the emissions coming from one of these two sectors for all regions and seasons. Industrial emissions (Fig. 5d) were relatively constant seasonally, with the strongest values in the South and the weakest typically in the East. Nonroad emissions (Fig. 5f), or emissions from offroad vehicles of all types, were higher in all regions in spring and summer, with the strongest values in the Midwest in all seasons. The commercial and residential sectors (Fig. 5e&g) exhibited the strongest, most consistent relative seasonal behaviors of all sectors. For both of these sectors, emissions were strongest in the winter and weakest in the summer in all regions. This can be explained by the shift from electrically powered air conditioning in the warmer seasons to FF-based heating in the cooler seasons. This is correlated with the rise in overall airborne $FF_{0.5\text{-}1\%}$ and $FF_{1\text{-}2\%}$ contributions, also peaking in the winter and at a minimum in the summer.

Regionally, residential and commercial emissions were much stronger during winter in the Mid-Atlantic and Midwest regions than in the South, likely due to the lower wintertime temperatures in those regions. However, this regional variability in the Vulcan sectors does not match the regional variability in the lower efficiency FF airborne NWF contributions, in particular where Midwestern NWF for $FF_{1\text{-}2\%}$ peaked in fall. One possible explanation could lie in the aforementioned agricultural harvesting equipment, which would fall under the Vulcan nonroad sector. Vulcan nonroad average emissions were weakest during fall, but if the combustion efficiency of these nonroad vehicles was underpredicted, this would have led to an underprediction in the respective CO_2 emissions.

352 4.2 Modeled CO_2 Fire Emissions Comparison

353 Similar to the Vulcan inventory data, CarbonTracker simulated fire emissions, resampled to the
354 WRF-Chem model grid, were subsampled along the ACT-America flight track at 5 s intervals
355 from the native 27 km^2 resolution pixels and for flight legs below 1 km AGL, then averaged
356 seasonally and by region (Fig. 6b). The largest modeled fire contribution in the Mid-Atlantic
357 region was during summer at ~10 mol CO_2/km^2*hr, with other seasons averaging less than 1/3 the
358 fire emissions of summer. Midwestern modeled fire average contributions were highest in spring
359 at ~7.5 mol CO_2/km^2*hr, with emissions in other seasons weaker by an order of magnitude. The
360 Southern region had the highest overall average fire emissions during the fall, winter, and spring
361 seasons, ranging from 18.5 - 20 mol CO_2/km^2*hr, with a strong drop during summer to ~6 mol
362 CO_2/km^2*hr.

363 As the airborne $\Delta CO/\Delta CO_2$ analysis calculated relative CO_2 contributions from BB compared to
364 overall combustion, the magnitude of these emissions cannot be directly compared to the modeled
365 fire contribution. To form a better means of comparison, Fig. 6c shows the same average modeled
366 fire CO_2 emissions as in Fig. 5b, but normalized by the average Vulcan modeled total FF CO_2
367 emissions in each region and season in order to account for variability in overall FF emission.
368 These FF-normalized modeled fire emission ratios (Fire/FF) can then be compared with a similar
369 ratio from the airborne data (Fig. 6a), which normalizes contributions from $BB_{>4\%}$ to those
370 attributed to FF combustion:

371 $$\frac{BB_{>4\%}}{\sum FF} = \frac{BB_{>4\%}}{FF_{0-0.5\%}+FF_{0.5-1\%}+FF_{1-2\%}+FF_{2-4\%}} \quad (2)$$

372 The airborne $BB_{>4\%}/\Sigma FF$ ratio values were near-zero for all regions in the summer, and during fall,
373 the values only exceed 0.5% in the Midwest. Comparably high $BB_{>4\%}/\Sigma FF$ ratios were observed
374 in the South during winter and spring, low ratios were observed in the Mid-Atlantic region in both
375 seasons and the Midwestern spring, whereas Midwestern winter ratios were between the two.

376 The modeled Fire/FF ratios captured the high airborne $BB_{>4\%}/\Sigma FF$ ratios during winter and spring
377 in the South compared to other regions. However, there are three major discrepancies to highlight.
378 The largest discrepancy is the high Fire/FF emission ratio predicted by the model in the South
379 during fall. The modeled fall:winter emission ratio was ~105%, while the airborne fall:winter fire

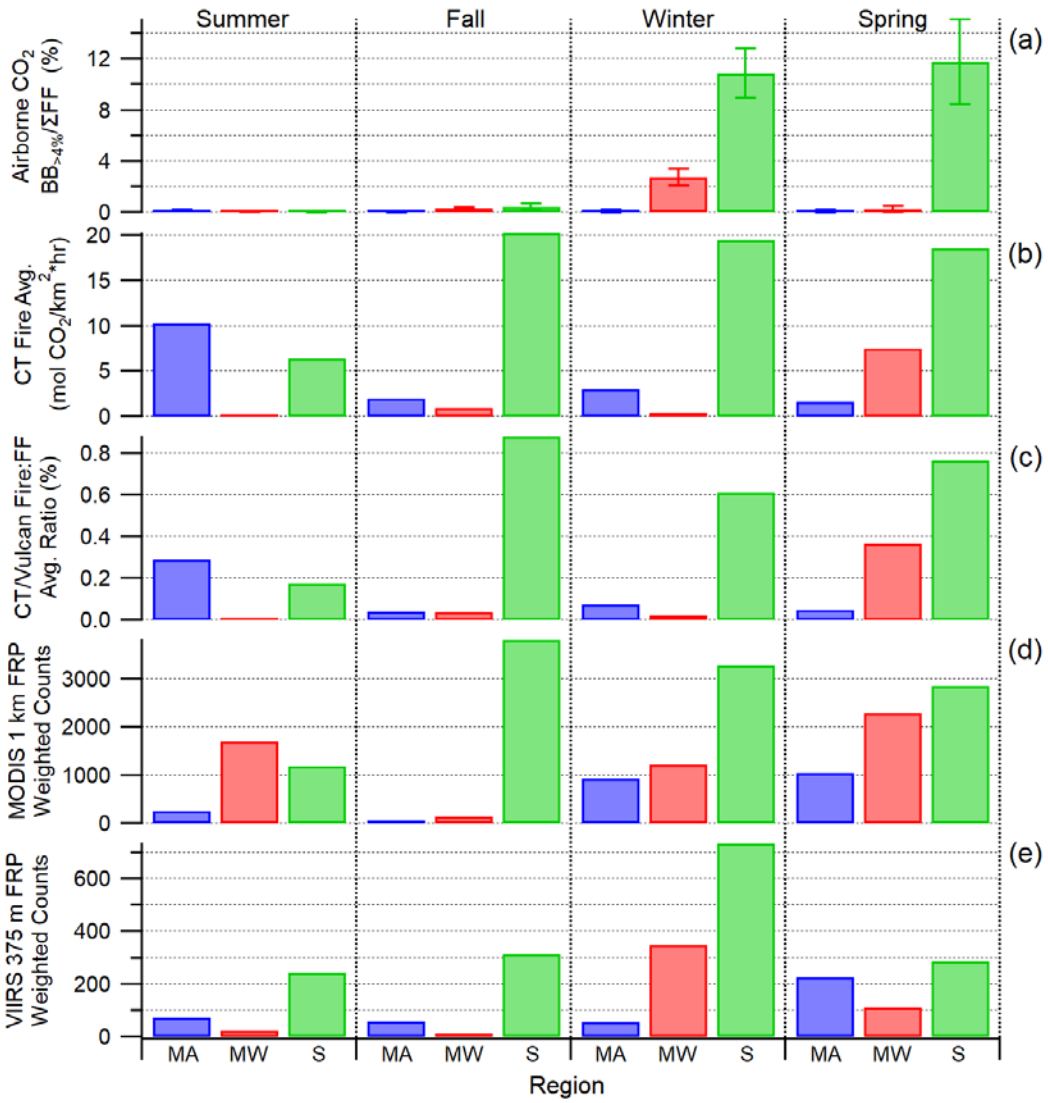

Figure 6. (a) Ratio of NWF contributions from $BB_{>4\%}$ to ΣFF from airborne analysis by region and season in PBL (< 1 km AGL). Error bars denote 1σ variability from sensitivity analysis. (b) CarbonTracker modeled fire emissions along aircraft flight track. (c) Ratio of CarbonTracker modeled fire emissions to Vulcan FF emissions along flight track. (d) Summed MODIS 1 km FRP-weighted fire counts within 50 km of flight track at < 1 km AGL altitude separated by season and region. (e) Summed VIIRS 375 m FRP-weighted fire counts within 14 km of flight track at < 1 km AGL altitude separated by season and region.

emission ratio was only 4 ± 2%. Another strong discrepancy was the relative winter and spring emission ratios in the Midwest, where the modeled winter:spring ratio was ~6% while the opposite was true for the airborne data, with a spring:winter emission ratio of 11 ± 10% due to the near lack of observed fire emissions in the spring. The final major discrepancy was the marked abundance of modeled emissions in the summer in both the Mid-Atlantic and Southern regions, as the airborne $BB_{>4\%}$/ΣFF ratios were negligible during that season in all three regions.

4.3 MODIS and VIIRS Fire Data

As the modeled fire product is parameterized using MODIS 1° fire counts (Jacobson et al., 2020), examining trends in satellite fire count could help understand the differences between the modeled results and aircraft observations. MODIS 1 km (FIRMS, 2020a) and VIIRS-SNPP 375 m (FIRMS, 2020b) data products were analyzed over each ACT-America campaign season and region. Data were filtered for flight days and aircraft altitudes below 1 km AGL. For MODIS, data were filtered for fires detected within 50 km (~ ±0.5°) of the aircraft flight tracks, the same resolution as the product used to drive the CarbonTracker fire emissions. For VIIRS, data were filtered for fires detected within 14 km of the aircraft flight tracks, comparable to the 27 km^2 resolution of the WRF-Chem model, in order to test the potential effects of spatial resolution. In addition to the fire counts, which denote the presence of fire, another product is fire radiative power (FRP), which is a measure of the irradiative intensity of the fire. FRP is used by models to determine the amount of combusted organic matter, and thus should scale with CO_2 emission (Kaiser et al., 2012). To account for this effect, Fig. 6d-e summarize the FRP-weighted sum of fire counts from each instrument by season and region for MODIS and VIIRS, respectively, while Fig. S4-5 show the full spatial distribution of the fire counts and FRP. This is a much simplified approach to methods described in the literature used to translate FRP to gas emissions, but the use here is to use this data as tool to provide insight into the model/airborne agreement.

Broadly, the MODIS fire products agreed well with the WRF-Chem/CarbonTracker fire product (Fig. 6b). The highest number of fire counts were in the South for all seasons, and there were many fewer counts in the South during summer compared to the other seasons, both matching the modeled fire emissions. One of the biggest discrepancies between MODIS and the modeled fire emissions was during summer. While the modeled fire emissions were highest in the Mid-Atlantic region during summer, the MODIS weighted counts were lowest in the Mid-Atlantic. Additionally, the modeled fire emissions in the Midwest during winter were a factor of ~7 smaller compared to those from the Mid-Atlantic region, and the two regions had comparable MODIS weighted counts. The causes for this may be attributable to differences in the very simple FRP weighting approach used here and the more complex analysis performed by the GFED and CASA modules.

Results using the VIIRS weighted counts were significantly different from MODIS. The ratio of Southern spring:winter weighted counts was ~90% from MODIS compared to ~40% from VIIRS,

and the ratio of Southern fall:winter weighted counts dropped from ~115% from MODIS to ~45% from VIIRS. Additionally, the ratio of winter:spring weighted counts in the Midwest increased from ~55% with MODIS to ~300% with VIIRS. As two of the largest discrepancies between the modeled and airborne emissions were the modeled high emissions in the South during fall and the ratio of winter:spring emissions in the Midwest, these shifts provide some circumstantial evidence that spatial resolution of either the satellite product or model may be contributing to those discrepancies.

5 Conclusions

In this study, we used airborne measurements of CO and CO_2 in the PBL to examine the relative frequency of regional and seasonal CO_2 contributions with various CE over the central and eastern US through weighted sliding correlations. Very high CE contributions ($\Delta CO/\Delta CO_2 < 0.5\%$) were found to be dominant during summer with negligible BB influence in all regions, which were attributed to highly-efficient FF combustion. The distribution in other seasons shifted moderately toward mid-range CE contributions ($\Delta CO/\Delta CO_2$ of 0.5-2%), peaking in winter overall. This was potentially due to the increased use of agricultural equipment during harvest and planting as well as FF combustion from increased indoor heating. The latter was supported by analysis of Vulcan v3 CO_2 emission inventory data, which showed similar seasonal behavior in residential and commercial FF CO_2 emission contributions.

Based on the airborne observations, PBL CO_2 BB emission contributions ($\Delta CO/\Delta CO_2 > 4\%$) relative to FF were seen strongest in South in winter and spring, with Mid-Atlantic BB contributions very low or negligible for all seasons. Modeled CO_2 fire/FF emissions agreed with these high relative fire emissions in the South, but also predicted enhanced fire/FF emissions in the South during fall, in the Midwest during spring, and in the Mid-Atlantic region in the summer. Analysis of FRP-weighted satellite showed that while the 1 km MODIS fire data averaged to 1° more accurately reproduced the modeled fire emissions, the 375 m VIIRS fire data averaged to 28 km reduced the overpredictions during the Southern fall and Midwestern spring. This suggests that the spatial resolution of the satellite products driving the model affects the measurement/model discrepancy, though does not explain the discrepancy in the Mid-Atlantic summer. These results imply that a combination of factors, such as undetected smaller fires below satellite product resolution or insufficiently constrained biosphere data, may cause significant biases in predictions

of BB CO_2 emissions in the US. Additionally, as air quality models use similar modules to drive BB VOC and CO emissions, these same biases would likely affect predictions of regional air quality as well.

Acknowledgments and Data

The Atmospheric Carbon and Transport (ACT)-America project is a NASA Earth Venture Suborbital-2 project funded by NASA's Earth Science Division (Grant NNX15AG76G to Penn State). Co-author SP was supported by NASA Grant Number 80NSSC19K0730 and Texas Tech University. We would like to thank James Plant, James Geiger, and Ali Aknan for their assistance with in situ instrument payload preparation and data collection. Thanks to Michael Obland, Byron Meadows, and Bing Lin for mission support and coordination. Thanks to NASA Wallops Flight Facility and NASA Langley Research Center for aircraft operations and logistics support. Thanks to Melissa Yang and BAER/NSRC for aircraft navigational and meteorological data support. Thanks to Duncan Aviation and TAC Air for FBO and logistics support during the ACT-America campaigns. We acknowledge the use of data from the NASA FIRMS application (https://firms.modaps.eosdis.nasa.gov/) operated by the NASA Goddard Space Flight Center Earth Science Data and Information System (ESDIS) project. All data are available from publicly accessible archives: https://doi.org/10.3334/ORNLDAAC/1593 (aircraft) and https://doi.org/10.26208/49kd-b637 (model).

References

Akagi, S. K., Yokelson, R. J., Wiedinmyer, C., Alvarado, M. J., Reid, J. S., Karl, T., Crounse, J. D., & Wennberg, P. O. (2011). Emission factors for open and domestic biomass burning for use in atmospheric models. *Atmospheric Chemistry and Physics*, *11*(9), 4039–4072. https://doi.org/10.5194/acp-11-4039-2011

Andreae, M. O., & Merlet, P. (2001). Emission of trace gases and aerosols from biomass burning. *Global Biogeochemical Cycles*, *15*(4), 955–966. https://doi.org/10.1029/2000GB001382

Baier, B. C., Sweeney, C., Choi, Y., Davis, K. J., DiGangi, J. P., Feng, S., Fried, A., Halliday, H., Higgs, J., Lauvaux, T., Miller, B. R., Montzka, S. A., Newberger, T., Nowak, J. B., Patra, P., Richter, D., Walega, J., & Weibring, P. (2020). Multispecies Assessment of Factors Influencing Regional and Enhancements During the Winter 2017 ACT-America Campaign. *Journal of Geophysical Research: Atmospheres*, *125*(2), e2019JD031339. https://doi.org/10.1029/2019JD031339

Ban-Weiss, G. A., McLaughlin, J. P., Harley, R. A., Kean, A. J., Grosjean, E., & Grosjean, D. (2008). Carbonyl and Nitrogen Dioxide Emissions From Gasoline- and Diesel-Powered Motor Vehicles. *Environmental Science & Technology*, *42*(11), 3944–3950. https://doi.org/10.1021/es8002487

Bell, E., O'Dell, C. W., Davis, K. J., Campbell, J., Browell, E., Denning, A. S., Dobler, J., Erxleben, W., Fan, T.-F., Kooi, S., Lin, B., Pal, S., & Weir, B. (2020). Evaluation of OCO-2 X_{CO2} Variability at Local and Synoptic Scales using Lidar and In Situ Observations from the ACT-America Campaigns. *Journal of Geophysical Research: Atmospheres*, *125*(10), e2019JD031400. https://doi.org/10.1029/2019JD031400

Bishop, G. A., & Stedman, D. H. (1990). On-road carbon monoxide emission measurement comparisons for the 1988-1989 Colorado oxy-fuels program. *Environmental Science & Technology*, *24*(6), 843–847. https://doi.org/10.1021/es00076a008

Butler, M. P., Lauvaux, T., Feng, S., Liu, J., Bowman, K. W., & Davis, K. J. (2020). Atmospheric Simulations of Total Column CO_2 Mole Fractions from Global to Mesoscale within the Carbon Monitoring System Flux Inversion Framework. *Atmosphere*, *11*(8), 787. https://doi.org/10.3390/atmos11080787

Campbell, J. F., Lin, B., Dobler, J., Pal, S., Davis, K., Obland, M. D., Erxleben, W., McGregor, D., O'Dell, C., Bell, E., Weir, B., Fan, T.-F., Kooi, S., Gordon, I., Corbett, A., & Kochanov, R. (2020). Field Evaluation of Column CO_2 Retrievals From Intensity-Modulated Continuous-Wave Differential Absorption Lidar Measurements During the ACT-America Campaign. *Earth and Space Science*, *7*(12), e2019EA000847. https://doi.org/10.1029/2019EA000847

Davis, K. J., Obland, M. D., Lin, B., Lauvaux, T., O'dell, C., Meadows, B., Browell, E. V., Digangi, J. P., Sweeney, C., Mcgill, M. J., Barrick, J. D., Nehrir, A. R., Yang, M. M., Bennett, J. R., Baier, B. C., Roiger, A., Pal, S., Gerken, T., Fried, A., … Pauly, R. M. (2018). ACT-America: L3 Merged In Situ Atmospheric Trace Gases and Flask Data, Eastern USA. *ORNL DAAC*. https://doi.org/10.3334/ORNLDAAC/1593

Davis, Kenneth J., Browell, E. V., Feng, S., Lauvaux, T., Obland, M. D., Pal, S., Baier, B. C., Baker, D., Baker, I., Barkley, Z. R., Bowman, K. W., Cui, Y., Denning, A. S., DiGangi, J. P., Dobler, J., Fried, A., Gerken, T., Keller, K., Lin, B., … Williams, C. (2020). The

Atmospheric Carbon and Transport (ACT) – America NASA Earth Venture Suborbital Mission. *Bulletin of the American Meteorological Society, in review*.

Djuricin, S., Pataki, D. E., & Xu, X. (2010). A comparison of tracer methods for quantifying CO_2 sources in an urban region. *Journal of Geophysical Research: Atmospheres*, *115*(D11). https://doi.org/10.1029/2009JD012236

Dlugokencky, E. J., Myers, R. C., Lang, P. M., Masarie, K. A., Crotwell, A. M., Thoning, K. W., Hall, B. D., Elkins, J. W., & Steele, L. P. (2005). Conversion of NOAA atmospheric dry air CH_4 mole fractions to a gravimetrically prepared standard scale. *Journal of Geophysical Research: Atmospheres*, *110*(D18). https://doi.org/10.1029/2005JD006035

Eldering, A., Wennberg, P. O., Crisp, D., Schimel, D. S., Gunson, M. R., Chatterjee, A., Liu, J., Schwandner, F. M., Sun, Y., O'Dell, C. W., Frankenberg, C., Taylor, T., Fisher, B., Osterman, G. B., Wunch, D., Hakkarainen, J., Tamminen, J., & Weir, B. (2017). The Orbiting Carbon Observatory-2 early science investigations of regional carbon dioxide fluxes. *Science*, *358*(6360). https://doi.org/10.1126/science.aam5745

Feng, S., Lauvaux, T., Davis, K. J., Keller, K., Zhou, Y., Williams, C., Schuh, A. E., Liu, J., & Baker, I. (2019a). Seasonal Characteristics of Model Uncertainties From Biogenic Fluxes, Transport, and Large-Scale Boundary Inflow in Atmospheric CO_2 Simulations Over North America. *Journal of Geophysical Research: Atmospheres*, *124*(24), 14325–14346. https://doi.org/10.1029/2019JD031165

Feng, S., Lauvaux, T., Keller, K., Davis, K. J., Rayner, P., Oda, T., & Gurney, K. R. (2019b). A Road Map for Improving the Treatment of Uncertainties in High-Resolution Regional

Carbon Flux Inverse Estimates. *Geophysical Research Letters*, *46*(22), 13461–13469. https://doi.org/10.1029/2019GL082987

FIRMS. (2020a). *MODIS/Aqua+Terra Thermal Anomalies/Fire locations 1km FIRMS V006*. http://doi.org/10.5067/FIRMS/MODIS/MCD14ML

FIRMS. (2020b). *VIIRS (S-NPP) I Band 375 m Active Fire Product NRT (Vector data)*. http://doi.org/10.5067/FIRMS/VIIRS/VNP14IMGT_NRT.002

Giglio, L., Randerson, J. T., & Werf, G. R. van der. (2013). Analysis of daily, monthly, and annual burned area using the fourth-generation global fire emissions database (GFED4). *Journal of Geophysical Research: Biogeosciences*, *118*(1), 317–328. https://doi.org/10.1002/jgrg.20042

Graven, H. D., Stephens, B. B., Guilderson, T. P., Campos, T. L., Schimel, D. S., Campbell, J. E., & Keeling, R. F. (2009). Vertical profiles of biospheric and fossil fuel-derived CO_2 and fossil fuel CO_2:CO ratios from airborne measurements of Δ14C, CO_2 and CO above Colorado, USA. *Tellus B: Chemical and Physical Meteorology*, *61*(3), 536–546. https://doi.org/10.1111/j.1600-0889.2009.00421.x

Griffin, R. J., Chen, J., Carmody, K., Vutukuru, S., & Dabdub, D. (2007). Contribution of gas phase oxidation of volatile organic compounds to atmospheric carbon monoxide levels in two areas of the United States. *Journal of Geophysical Research: Atmospheres*, *112*(D10). https://doi.org/10.1029/2006JD007602

Gurney, K. R., Liang, J., Patarasuk, R., Song, Y., Huang, J., & Roest, G. (2020b). Vulcan: High-Resolution Annual Fossil Fuel CO_2 Emissions in USA, 2010-2015, Version 3. *ORNL DAAC*. https://doi.org/10.3334/ORNLDAAC/1741

Gurney, Kevin R., Liang, J., Patarasuk, R., Song, Y., Huang, J., & Roest, G. (2020a). The Vulcan Version 3.0 High-Resolution Fossil Fuel CO_2 Emissions for the United States. *Journal of Geophysical Research: Atmospheres*, *125*(19), e2020JD032974. https://doi.org/10.1029/2020JD032974

Halliday, H. S., DiGangi, J. P., Choi, Y., Diskin, G. S., Pusede, S. E., Rana, M., Nowak, J. B., Knote, C., Ren, X., He, H., Dickerson, R. R., & Li, Z. (2019). Using Short-Term CO/CO_2 Ratios to Assess Air Mass Differences Over the Korean Peninsula During KORUS-AQ. *Journal of Geophysical Research: Atmospheres*, *124*(20), 10951–10972. https://doi.org/10.1029/2018JD029697

Holloway, T., Levy, H., & Kasibhatla, P. (2000). Global distribution of carbon monoxide. *Journal of Geophysical Research: Atmospheres*, *105*(D10), 12123–12147. https://doi.org/10.1029/1999JD901173

Jacobson, A. R., Schuldt, K. N., Miller, J. B., Oda, T., Tans, P., Andrews, A., Mund, J., Ott, L., Collatz, G. J., Aalto, T., Afshar, S., Aikin, K., Aoki, S., Apadula, F., Baier, B., Bergamaschi, P., Beyersdorf, A., Biraud, S. C., Bollenbacher, A., … Zimnoch, M. (2020). *CarbonTracker CT2019*. https://doi.org/10.25925/39M3-6069

Kaiser, J. W., Heil, A., Andreae, M. O., Benedetti, A., Chubarova, N., Jones, L., Morcrette, J.-J., Razinger, M., Schultz, M. G., Suttie, M., & van der Werf, G. R. (2012). Biomass burning

emissions estimated with a global fire assimilation system based on observed fire radiative power. *Biogeosciences*, *9*(1), 527–554. https://doi.org/10.5194/bg-9-527-2012

Kostinek, J., Roiger, A., Davis, K. J., Sweeney, C., DiGangi, J. P., Choi, Y., Baier, B., Hase, F., Groß, J., Eckl, M., Klausner, T., & Butz, A. (2019). Adaptation and performance assessment of a quantum and interband cascade laser spectrometer for simultaneous airborne in situ observation of CH_4, C_2H_6, CO_2, CO and N_2O. *Atmospheric Measurement Techniques*, *12*(3), 1767–1783. https://doi.org/10.5194/amt-12-1767-2019

LaFranchi, B. W., Pétron, G., Miller, J. B., Lehman, S. J., Andrews, A. E., Dlugokencky, E. J., Hall, B., Miller, B. R., Montzka, S. A., Neff, W., Novelli, P. C., Sweeney, C., Turnbull, J. C., Wolfe, D. E., Tans, P. P., Gurney, K. R., & Guilderson, T. P. (2013). Constraints on emissions of carbon monoxide, methane, and a suite of hydrocarbons in the Colorado Front Range using observations of $^{14}CO_2$. *Atmospheric Chemistry and Physics*, *13*(21), 11101–11120. https://doi.org/10.5194/acp-13-11101-2013

Lauvaux, T., Schuh, A. E., Uliasz, M., Richardson, S., Miles, N., Andrews, A. E., Sweeney, C., Diaz, L. I., Martins, D., Shepson, P. B., & Davis, K. J. (2012). Constraining the CO_2 budget of the corn belt: Exploring uncertainties from the assumptions in a mesoscale inverse system. *Atmospheric Chemistry and Physics*, *12*(1), 337–354. https://doi.org/10.5194/acp-12-337-2012

McCarty, J. L., Justice, C. O., & Korontzi, S. (2007). Agricultural burning in the Southeastern United States detected by MODIS. *Remote Sensing of Environment*, *108*(2), 151–162. https://doi.org/10.1016/j.rse.2006.03.020

589 Middlebrook, A. M., Murphy, D. M., Ahmadov, R., Atlas, E. L., Bahreini, R., Blake, D. R.,
590 Brioude, J., Gouw, J. A. de, Fehsenfeld, F. C., Frost, G. J., Holloway, J. S., Lack, D. A.,
591 Langridge, J. M., Lueb, R. A., McKeen, S. A., Meagher, J. F., Meinardi, S., Neuman, J.
592 A., Nowak, J. B., … Ravishankara, A. R. (2012). Air quality implications of the Deepwater
593 Horizon oil spill. *Proceedings of the National Academy of Sciences*, *109*(50), 20280–
594 20285. https://doi.org/10.1073/pnas.1110052108

595 Novelli, P. C., Elkins, J. W., & Steele, L. P. (1991). The development and evaluation of a
596 gravimetric reference scale for measurements of atmospheric carbon monoxide. *Journal of*
597 *Geophysical Research: Atmospheres*, *96*(D7), 13109–13121.
598 https://doi.org/10.1029/91JD01108

599 Pal, S., Davis, K. J., Lauvaux, T., Browell, E. V., Gaudet, B. J., Stauffer, D. R., Obland, M. D.,
600 Choi, Y., DiGangi, J. P., Feng, S., Lin, B., Miles, N. L., Pauly, R. M., Richardson, S. J., &
601 Zhang, F. (2020). Observations of Greenhouse Gas Changes Across Summer Frontal
602 Boundaries in the Eastern United States. *Journal of Geophysical Research: Atmospheres*,
603 *125*(5), e2019JD030526. https://doi.org/10.1029/2019JD030526

604 Peischl, J., Ryerson, T. B., Holloway, J. S., Parrish, D. D., Trainer, M., Frost, G. J., Aikin, K. C.,
605 Brown, S. S., Dubé, W. P., Stark, H., & Fehsenfeld, F. C. (2010). A top-down analysis of
606 emissions from selected Texas power plants during TexAQS 2000 and 2006. *Journal of*
607 *Geophysical Research: Atmospheres*, *115*(D16). https://doi.org/10.1029/2009JD013527

608 Peters, W., Miller, J. B., Whitaker, J., Denning, A. S., Hirsch, A., Krol, M. C., Zupanski, D.,
609 Bruhwiler, L., & Tans, P. P. (2005). An ensemble data assimilation system to estimate CO_2

surface fluxes from atmospheric trace gas observations. *Journal of Geophysical Research: Atmospheres*, *110*(D24). https://doi.org/10.1029/2005JD006157

Reum, F., Gerbig, C., Lavric, J. V., Rella, C. W., & Göckede, M. (2019). Correcting atmospheric CO_2 and CH_4 mole fractions obtained with Picarro analyzers for sensitivity of cavity pressure to water vapor. *Atmospheric Measurement Techniques*, *12*(2), 1013–1027. https://doi.org/10.5194/amt-12-1013-2019

Silva, S. J., Arellano, A. F., & Worden, H. M. (2013). Toward anthropogenic combustion emission constraints from space-based analysis of urban CO_2/CO sensitivity. *Geophysical Research Letters*, *40*(18), 4971–4976. https://doi.org/10.1002/grl.50954

Smith, M. L., Kort, E. A., Karion, A., Sweeney, C., Herndon, S. C., & Yacovitch, T. I. (2015). Airborne Ethane Observations in the Barnett Shale: Quantification of Ethane Flux and Attribution of Methane Emissions. *Environmental Science & Technology*, *49*(13), 8158–8166. https://doi.org/10.1021/acs.est.5b00219

Suntharalingam, P., Jacob, D. J., Palmer, P. I., Logan, J. A., Yantosca, R. M., Xiao, Y., Evans, M. J., Streets, D. G., Vay, S. L., & Sachse, G. W. (2004). Improved quantification of Chinese carbon fluxes using CO_2/CO correlations in Asian outflow. *Journal of Geophysical Research: Atmospheres*, *109*(D18), n/a–n/a. https://doi.org/10.1029/2003JD004362

Tans, P. P., Crotwell, A. M., & Thoning, K. W. (2017). Abundances of isotopologues and calibration of CO_2 greenhouse gas measurements. *Atmos. Meas. Tech.*, *10*(7), 2669–2685. https://doi.org/10.5194/amt-10-2669-2017

Turnbull, J. C., Karion, A., Fischer, M. L., Faloona, I., Guilderson, T., Lehman, S. J., Miller, B. R., Miller, J. B., Montzka, S., Sherwood, T., Saripalli, S., Sweeney, C., & Tans, P. P. (2011). Assessment of fossil fuel carbon dioxide and other anthropogenic trace gas emissions from airborne measurements over Sacramento, California in spring 2009. *Atmospheric Chemistry and Physics*, *11*(2), 705–721. https://doi.org/10.5194/acp-11-705-2011

Turnbull, Jocelyn C., Sweeney, C., Karion, A., Newberger, T., Lehman, S. J., Tans, P. P., Davis, K. J., Lauvaux, T., Miles, N. L., Richardson, S. J., Cambaliza, M. O., Shepson, P. B., Gurney, K., Patarasuk, R., & Razlivanov, I. (2015). Toward quantification and source sector identification of fossil fuel CO_2 emissions from an urban area: Results from the INFLUX experiment. *Journal of Geophysical Research: Atmospheres*, *120*(1), 292–312. https://doi.org/10.1002/2014JD022555

USEPA. (2010). *AP 42, Fifth Edition Compilation of Air Pollutant Emissions Factors: Vol. 1: Stationary Point and Area Sources*. USEPA (United States Environmental Protection Agency).

van der Werf, G. R., Randerson, J. T., Giglio, L., van Leeuwen, T. T., Chen, Y., Rogers, B. M., Mu, M., van Marle, M. J. E., Morton, D. C., Collatz, G. J., Yokelson, R. J., & Kasibhatla, P. S. (2017). Global fire emissions estimates during 1997–2016. *Earth System Science Data*, *9*(2), 697–720. https://doi.org/10.5194/essd-9-697-2017

Venkataraman, C., & Rao, G. U. M. (2001). Emission Factors of Carbon Monoxide and Size-Resolved Aerosols from Biofuel Combustion. *Environmental Science & Technology*, *35*(10), 2100–2107. https://doi.org/10.1021/es001603d

Wei, Y., Shrestha, R., & McNelis, J. (2020). The ACT-America Datasets: Description, Management and Delivery. *Earth and Space Science*, *in prep*.

Weibring, P., Richter, D., Walega, J. G., Fried, A., DiGangi, J., Halliday, H., Choi, Y., Baier, B., Sweeney, C., Miller, B., Davis, K. J., Barkley, Z., & Obland, M. D. (2020). Autonomous Airborne Mid-IR Spectrometer for High Precision Measurements of Ethane during the NASA ACT-America Studies. *Atmospheric Measurement Techniques Discussions*, 1–42. https://doi.org/10.5194/amt-2020-210

Wu, C., & Yu, J. Z. (2018). Evaluation of linear regression techniques for atmospheric applications: The importance of appropriate weighting. *Atmospheric Measurement Techniques*, *11*(2), 1233–1250. https://doi.org/10.5194/amt-11-1233-2018

Yokota, T., Yoshida, Y., Eguchi, N., Ota, Y., Tanaka, T., Watanabe, H., & Maksyutov, S. (2009). Global concentrations of CO_2 and CH_4 retrieved from GOSAT: First preliminary results. *Scientific Online Letters on the Atmosphere*, *5*(1), 160–163. https://doi.org/10.2151/sola.2009-041